Supplementary Material for "Nonreciprocal Superradiant Phase Transitions and Multicriticality in a Cavity QED System"

Gui-Lei Zhu,[1, 2] Chang-Sheng Hu,[3] Hui Wang,[2] Wei Qin,[2, 4] Xin-You Lü,[5, *] and Franco Nori[2, 6, 7, †]

[1]*Department of Physics, Zhejiang Sci-Tech University, Hangzhou 310018, China*
[2]*Theoretical Quantum Physics Laboratory, Cluster for Pioneering Research, RIKEN, Wakoshi, Saitama 351-0198, Japan*
[3]*Department of Physics, Anhui Normal University, Wuhu 241000, China*
[4]*Center for Joint Quantum Studies and Department of Physics,*
School of Science, Tianjin University, Tianjin 300350, China
[5]*School of Physics, Huazhong University of Science and Technology*
and Wuhan Institute of Quantum Technology, Wuhan 430074, China
[6]*Quantum Computing Center, RIKEN, Wakoshi, Saitama 351-0198, Japan*
[7]*Department of Physics, The University of Michigan, Ann Arbor, MI, 48109-1040, USA*
(Dated: March 26, 2024)

Contents

*Electronic address: xinyoulu@hust.edu.cn
†Electronic address: fnori@riken.jp

S1. MEAN-FIELD SOLUTIONS OF α AND β

We recall that the system Hamiltonian in the forward pump reads,

$$H = (\Delta + \Delta_F)a^\dagger a + \frac{\Delta_q}{2}\sigma_z + g_a(a\sigma_+ + a^\dagger\sigma_-) + G(a^{\dagger 2} + a^2)$$
$$+ (\Delta - \Delta_F)b^\dagger b + g_b(b\sigma_+ + b^\dagger\sigma_-) + J(a^\dagger b + b^\dagger a), \tag{S1}$$

where a and b are the annihilation operators for the counterclockwise and clockwise cavity modes, respectively. Also, $\sigma_\pm = (\sigma_x + i\sigma_y)/2$, and $\sigma_{x,y,z}$ are Pauli matrices of the two-level atom. Here, Δ_F is the Sagnac shift caused by the rotation of the cavity. The counterclockwise and clockwise cavity modes are coupled to the atom with the strengths g_a and g_b, respectively. By employing the master equation (2) shown in the main text, we can derive the Heisenberg equations of motion for operators,

$$\frac{da}{dt} = -i(\Delta + \Delta_F)a - \kappa a - 2iGa^\dagger - iJb - \frac{i}{2}g_a\sigma_x - \frac{1}{2}g_a\sigma_y, \tag{S2}$$

$$\frac{db}{dt} = -i(\Delta - \Delta_F)b - \kappa b - iJa - \frac{i}{2}g_b\sigma_x - \frac{1}{2}g_b\sigma_y, \tag{S3}$$

$$\frac{d\sigma_x}{dt} = -\Delta_q\sigma_y + ig_a(a - a^\dagger)\sigma_z + ig_b(b - b^\dagger)\sigma_z, \tag{S4}$$

$$\frac{d\sigma_y}{dt} = \Delta_q\sigma_x - g_a(a + a^\dagger)\sigma_z - g_b(b + b^\dagger)\sigma_z, \tag{S5}$$

$$\frac{d\sigma_z}{dt} = ig_a(a^\dagger - a)\sigma_x + ig_b(b^\dagger - b)\sigma_x + g_a(a + a^\dagger)\sigma_y + g_b(b + b^\dagger)\sigma_y. \tag{S6}$$

In these equations, we assumed that the decay rates of cavity modes a and b are equal, namely, $\kappa_a = \kappa_b = \kappa$. Additionally, we neglected the atomic loss in the system. Similar to the standard Rabi model, in the steady-state limit, we set the following expectation values: $\langle\sigma_x\rangle = X$, $\langle\sigma_y\rangle = Y$, $\langle\sigma_z\rangle = Z$, $\langle a\rangle = \alpha\sqrt{\eta_+}$, $\langle b\rangle = \beta\sqrt{\eta_-}$, where

$$\eta_+ = \frac{\Delta_q}{\Delta + \Delta_F}, \quad \eta_- = \frac{\Delta_q}{\Delta - \Delta_F}. \tag{S7}$$

The mean-field approximation holds in the infinite detuning limit, where $\eta_\pm \to \infty$. The validity of the mean-field approximation is discussed in Sec. S6. Under the spin-conservation law, $X^2 + Y^2 + Z^2 = 1$, the following relations are obtained:

$$C = \Gamma_1\alpha_{\rm re}^2 + \Gamma_2\alpha_{\rm re}\alpha_{\rm im} + \Gamma_3\alpha_{\rm im}^2, \tag{S8}$$

$$C = K(\alpha_{\rm re}^2 + \alpha_{\rm im}^2), \tag{S9}$$

where $C = 1 - Z^2$,

$$\Gamma_{1,3} = \frac{[16(\Delta + \Delta_F \pm 2G)^2 + \kappa^2]}{(\Delta + \Delta_F)^2\lambda_a^2}, \quad \Gamma_2 = \frac{128G\kappa}{(\Delta + \Delta_F)^2\lambda_a^2}, \quad K = \frac{16[(\Delta - \Delta_F)^2 + \kappa^2]\lambda_a^2 Z^2}{16\kappa^2 + (\Delta - \Delta_F)^2(4 + \lambda_b^2 Z^2)}. \tag{S10}$$

In these equations, we have separated the real and imaginary parts of α and β as $\alpha = \alpha_{\rm re} + i\alpha_{\rm im}$ and $\beta = \beta_{\rm re} + i\beta_{\rm im}$. The constraint parameter Z satisfies

$$Z_\pm = 4\frac{-\Delta_+ h_1 - \Delta_- h_2 \pm \sqrt{[h_1(2G - \kappa) - \kappa h_2][h_1(2G + \kappa) + \kappa h_2]}}{\Delta_+ h_1\lambda_a^2 + 2\Delta_+\Delta_-(\Delta_+\Delta_- + \kappa^2)\lambda_a^2\lambda_b^2 + \Delta_- h_2\lambda_b^2}, \tag{S11}$$

where we have denoted $\Delta_\pm = \Delta \pm \Delta_F$, $h_1 = \Delta_+(\Delta_-^2 + \kappa^2)\lambda_a^2$ and $h_2 = \Delta_-(\Delta_+^2 - 4G^2 + \kappa^2)\lambda_b^2$ for simplification purposes.

The mean-field solutions of α and β in the steady state can be obtained by solving Eqs. (S8) and (S9). The solutions are given by

$$\alpha_{\mathrm{re}} = \pm\sqrt{C}\sqrt{\frac{\Gamma_2^2 - 2(\Gamma_1 - \Gamma_3)(\Gamma_3 - K) + \Gamma_2\sqrt{\Gamma_2^2 + 4(\Gamma_1 - K)(K - \Gamma_3)}}{2(\Gamma_2^2 + (\Gamma_1 - \Gamma_3)^2)K}}, \tag{S12}$$

$$\alpha_{\mathrm{im}} = \frac{\Gamma_2 - \sqrt{\Gamma_2^2 + 4(\Gamma_1 - K)(K - \Gamma_3)}}{2(K - \Gamma_3)}\alpha_{\mathrm{re}}, \tag{S13}$$

$$\beta_{\mathrm{re}} = -4\frac{(\Delta + \Delta_F + 2G)\alpha_{\mathrm{re}} + \kappa\alpha_{\mathrm{im}}}{(\Delta + \Delta_F)\lambda_a\lambda_b Z} - \frac{\lambda_a}{\lambda_b}\alpha_{\mathrm{re}}, \tag{S14}$$

$$\beta_{\mathrm{im}} = -4\frac{(\Delta + \Delta_F - 2G)\alpha_{\mathrm{im}} - \kappa\alpha_{\mathrm{re}}}{(\Delta + \Delta_F)\lambda_a\lambda_b Z} - \frac{\lambda_a}{\lambda_b}\alpha_{\mathrm{im}}. \tag{S15}$$

where we have defined the rescaled atom-field coupling strengths as $\lambda_a = 2g_a/\sqrt{(\Delta + \Delta_F)\Delta_q}$ and $\lambda_b = 2g_b/\sqrt{(\Delta - \Delta_F)\Delta_q}$.

S2. EFFECTIVE HAMILTONIAN IN THE INFINITE-DETUNING LIMIT $(\Delta_q/(\Delta \pm \Delta_F) \to \infty)$

In Sec. S1, we used the mean-field approximation to obtain the steady-state solutions of α and β, which neglected quantum fluctuations. In this section, we provide a full quantum description of the Hamiltonian.

A. Low-energy Hamiltonian in the normal phase

In the large detuning limit, where the atomic energy scale is much larger than the field part, we can decouple the atomic subspaces and focus on the lowest atomic subspace. This allows us to eliminate the atomic part and obtain the effective low-energy Hamiltonian. To achieve this, we rewrite Hamiltonian (S1) as

$$H = H_c + g_a V_a + g_b V_b, \tag{S16}$$

with

$$H_c = (\Delta + \Delta_F)a^\dagger a + \frac{\Delta_q}{2}\sigma_z + G(a^{\dagger 2} + a^2) + (\Delta - \Delta_F)b^\dagger b + J(a^\dagger b + b^\dagger a),$$

and

$$V_a = (a\sigma_+ + a^\dagger\sigma_-), \qquad V_b = (b\sigma_+ + b^\dagger\sigma_-).$$

The Hamiltonian H_c has two decoupled spin subspaces $\mathcal{H}_\downarrow$ and $\mathcal{H}_\uparrow$, where $|\uparrow\rangle$ and $|\downarrow\rangle$ are the eigenstates of σ_z. However, the Hamiltonian $g_a V_a + g_b V_b$ introduces the interactions between these two subspaces. To eliminate the interaction terms, we apply the Schrieffer-Woff transformation with the unitary operator $S_{\mathrm{np}} = g_a/\Delta_q(a^\dagger\sigma_- - a\sigma_+) + g_b/\Delta_q(b^\dagger\sigma_- - b\sigma_+)$ to the master equation given in Eq. (2) of the main text. We keep terms up to $g_{a,b}^2/\Delta_q$ and neglect higher-order terms in the large detuning limit, i.e., $\Delta_q/(\Delta \pm \Delta_F) \to \infty$ and $\Delta_q/G \to \infty$. Under the projection of the $\mathcal{H}_\downarrow$ space, we obtain the effective master equation in the normal phase,

$$\dot{\rho}_{\mathrm{np}} = -i[H_{\mathrm{np}}, \rho_{\mathrm{np}}] + \kappa(2a\rho_{\mathrm{np}}a^\dagger - a^\dagger a\rho_{\mathrm{np}} - \rho_{\mathrm{np}}a^\dagger a) + \kappa(2b\rho_{\mathrm{np}}b^\dagger - b^\dagger b\rho_{\mathrm{np}} - \rho_{\mathrm{np}}b^\dagger b), \tag{S17}$$

where $\rho_{\mathrm{np}} = \langle\downarrow|e^{-S_{\mathrm{np}}}\rho e^{S_{\mathrm{np}}}|\downarrow\rangle$, and the effective low-energy Hamiltonian in the normal phase becomes,

$$\begin{aligned} H_{\mathrm{np}} &\equiv \langle\downarrow|e^{-S_{\mathrm{np}}}He^{S_{\mathrm{np}}}|\downarrow\rangle \\ &= \Delta_a a^\dagger a + \Delta_b b^\dagger b + G(a^{\dagger 2} + a^2) + J_s(ab^\dagger + a^\dagger b) - \frac{\Delta_q}{2}, \end{aligned} \tag{S18}$$

where $\Delta_a = (\Delta + \Delta_F)(1 - \lambda_a^2/4)$, $\Delta_b = (\Delta - \Delta_F)(1 - \lambda_b^2/4)$, $J_s = J - \lambda_a\lambda_b\sqrt{(\Delta + \Delta_F)(\Delta - \Delta_F)}/4$ and the renormalized atom-field couplings $\lambda_a = 2g_a/\sqrt{(\Delta + \Delta_F)\Delta_q}$ and $\lambda_b = 2g_b/\sqrt{(\Delta - \Delta_F)\Delta_q}$.

B.   Low-energy Hamiltonian in the superradiant phase

To address the superradiant phase where the cavity fields are macroscopically occupied, we apply displacement transformations to cavity modes. Specifically, we have

$$D^\dagger[\alpha\sqrt{\eta_+}]aD[\alpha\sqrt{\eta_+}] = c + \alpha\sqrt{\eta_+}, \quad D^\dagger[\beta\sqrt{\eta_-}]bD[\beta\sqrt{\eta_-}] = d + \beta\sqrt{\eta_-} \tag{S19}$$

with $D[\alpha\sqrt{\eta_+}] = \exp[\sqrt{\eta_+}(\alpha a^\dagger - \alpha^* a)]$ and $D[\beta\sqrt{\eta_-}] = \exp[\sqrt{\eta_-}(\beta b^\dagger - \beta^* b)]$. Notably, the displacements α and β correspond to the mean-field solutions discussed in Sec. S1. Here, we use c and d to denote the fluctuation operators of the cavity modes. By applying the displacement transformation, the master equation becomes

$$\dot{\tilde{\rho}} = -i[H(\alpha, \beta), \tilde{\rho}] + \kappa(2c\tilde{\rho}c^\dagger - c^\dagger c\tilde{\rho} - \tilde{\rho}c^\dagger c) + \kappa(2d\tilde{\rho}d^\dagger - d^\dagger d\tilde{\rho} - \tilde{\rho}d^\dagger d), \tag{S20}$$

where $\tilde{\rho} = D^\dagger[\alpha\sqrt{\eta_+}]D^\dagger[\beta\sqrt{\eta_-}]\rho D[\alpha\sqrt{\eta_+}]D[\beta\sqrt{\eta_-}]$ and $H(\alpha, \beta)$ reads,

$$H(\alpha, \beta) = \Delta_+ c^\dagger c + \frac{\Delta_q}{2}\sigma_z + \Delta_- d^\dagger d + \frac{1}{2}\lambda_a\sqrt{\Delta_q\Delta_+}(c\sigma_+ + c^\dagger\sigma_-) + \frac{1}{2}\lambda_b\sqrt{\Delta_q\Delta_-}(d^\dagger\sigma_- + d\sigma_+)$$
$$+ G(c^{\dagger 2} + c^2) + J(c^\dagger d + d^\dagger c) + \frac{\Delta_q\lambda_a}{2}(\alpha\sigma_+ + \alpha^*\sigma_-) + \frac{\Delta_q\lambda_b}{2}(\beta\sigma_+ + \beta^*\sigma_-), \tag{S21}$$

where $\Delta_\pm = \Delta \pm \Delta_F$, $\alpha = \alpha_{\rm re} + i\alpha_{\rm im}$, $\beta = \beta_{\rm re} + i\beta_{\rm im}$ and we have omitted the linear terms and constant terms in the Hamiltonian.

Next, we focus on the atomic part of Hamiltonian, which includes terms such as $\Delta_q\sigma_z/2 + \Delta_q\lambda_a(\alpha\sigma_+ + \alpha^*\sigma_-)/2 + \Delta_q\lambda_b(\beta\sigma_+ + \beta^*\sigma_-)/2$. The eigenvalues of this atomic part are $\pm\tilde{\Delta}_q/2$, with

$$\tilde{\Delta}_q = \Delta_q\sqrt{1 + \lambda_a^2(\alpha_{\rm re}^2 + \alpha_{\rm im}^2) + 2\lambda_a\lambda_b(\alpha_{\rm im}\beta_{\rm im} + \alpha_{\rm re}\beta_{\rm re}) + \lambda_b^2(\beta_{\rm im}^2 + \beta_{\rm re}^2)}, \tag{S22}$$

and the corresponding eigenstates are given by

$$|\tilde{\downarrow}\rangle = \cos\theta e^{i\gamma}|\uparrow\rangle + \sin\theta e^{i\phi}|\downarrow\rangle, \tag{S23}$$
$$|\tilde{\uparrow}\rangle = -\sin\theta e^{-i\phi}|\uparrow\rangle + \cos\theta e^{-i\gamma}|\downarrow\rangle, \tag{S24}$$

where

$$e^{i\phi} = \frac{\lambda_a(\alpha_{\rm im} + i\alpha_{\rm re}) + \lambda_b(\beta_{\rm im} + i\beta_{\rm re})}{\sqrt{\lambda_a^2(\alpha_{\rm re}^2 + \alpha_{\rm im}^2) + 2\lambda_a\lambda_b(\alpha_{\rm im}\beta_{\rm im} + \alpha_{\rm re}\beta_{\rm re}) + \lambda_b^2(\beta_{\rm re}^2 + \beta_{\rm im}^2)}}, \tag{S25}$$

and $e^{i\gamma} = -i$. The angle θ satisfies

$$\tan 2\theta = -\sqrt{\lambda_a^2(\alpha_{\rm re}^2 + \alpha_{\rm im}^2) + 2\lambda_a\lambda_b(\alpha_{\rm im}\beta_{\rm im} + \alpha_{\rm re}\beta_{\rm re}) + \lambda_b^2(\beta_{\rm re}^2 + \beta_{\rm im}^2)}. \tag{S26}$$

Now, we define the Pauli matrices in the $\{|\tilde{\downarrow}\rangle, |\tilde{\uparrow}\rangle\}$ basis as $\tau_x = |\tilde{\uparrow}\rangle\langle\tilde{\downarrow}| + |\tilde{\downarrow}\rangle\langle\tilde{\uparrow}|$, $\tau_y = -i(|\tilde{\uparrow}\rangle\langle\tilde{\downarrow}| - |\tilde{\downarrow}\rangle\langle\tilde{\uparrow}|)$ and $\tau_z = |\tilde{\uparrow}\rangle\langle\tilde{\uparrow}| - |\tilde{\downarrow}\rangle\langle\tilde{\downarrow}|$. Then, $\sigma_{\pm, z}$ in terms of $\tau_{\pm, z}$ can be expressed as

$$\sigma_+ = -\sin\theta\cos\theta e^{i(\phi-\gamma)}\tau_z + \cos^2\theta e^{-2i\gamma}\tau_- - \sin^2\theta e^{2i\phi}\tau_+, \tag{S27}$$
$$\sigma_z = -\cos 2\theta\tau_z - \sin 2\theta e^{i(\phi+\gamma)}\tau_+ - \sin 2\theta e^{-i(\phi+\gamma)}\tau_-. \tag{S28}$$

By substituting the expression for $\sigma_\pm$ and σ_z from Eqs. (S27) and (S28) into the Hamiltonian equation (S21),we obtain

the transformed Hamiltonian as follows:

$$
\begin{aligned}
H(\alpha,\beta) = {} & \Delta_+ c^\dagger c + \Delta_- d^\dagger d + \frac{\tilde{\Delta}_q}{2}\tau_z + G(c^{\dagger 2} + c^2) + J(c^\dagger d + d^\dagger c) \\
& - \frac{1}{2}\lambda_a\sqrt{\Delta_q \Delta_+}\sin^2\theta(c\tau_+ e^{2i\phi} + c^\dagger\tau_- e^{-2i\phi}) - \frac{1}{2}\lambda_a\sqrt{\Delta_q \Delta_+}\cos^2\theta(c\tau_- + c^\dagger\tau_+) \\
& - \frac{1}{2}\lambda_b\sqrt{\Delta_q \Delta_-}\sin^2\theta(d\tau_+ e^{2i\phi} + d^\dagger\tau_- e^{-2i\phi}) - \frac{1}{2}\lambda_b\sqrt{\Delta_q \Delta_-}\cos^2\theta(d\tau_- + d^\dagger\tau_+).
\end{aligned}
\tag{S29}
$$

Next, we apply the unitary transformation $H'_{\mathrm{sp}} = e^{-S_{\mathrm{sp}}}H(\alpha,\beta)e^{S_{\mathrm{sp}}}$ with the operator S_{sp} given by:

$$
\begin{aligned}
S_{\mathrm{sp}} = {} & \frac{\lambda_a\sqrt{\Delta_q(\Delta + \Delta_F)}}{2\bar{\Delta}_q}\left[\sin^2\theta(c\tau_+ e^{2i\phi} - c^\dagger\tau_- e^{-2i\phi}) + \cos^2(c^\dagger\tau_+ - c\tau_-)\right] \\
& + \frac{\lambda_b\sqrt{\Delta_q(\Delta - \Delta_F)}}{2\bar{\Delta}_q}\left[\sin^2\theta(d\tau_+ e^{2i\phi} - d^\dagger\tau_- e^{-2i\phi}) + \cos^2\theta(d^\dagger\tau_+ - d\tau_-)\right].
\end{aligned}
\tag{S30}
$$

Projecting H'_{sp} onto $|\tilde{\downarrow}\rangle$ basis, we obtain the effective Hamiltonian in the superradiant phase

$$
\begin{aligned}
H_{\mathrm{sp}} = {} & \Lambda_1 c^\dagger c + \Lambda_2 d^\dagger d + G(c^2 + c^{\dagger 2}) + \Lambda_3(cd^\dagger + c^\dagger d) + \Lambda_4(e^{2i\phi}c^2 + e^{-2i\phi}c^{\dagger 2}) \\
& + \Lambda_5(e^{2i\phi}d^2 + e^{-2i\phi}d^{\dagger 2}) + \Lambda_6(e^{2i\phi}cd + e^{-2i\phi}c^\dagger d^\dagger),
\end{aligned}
\tag{S31}
$$

where

$$
\begin{aligned}
\Lambda_1 &= (\Delta + \Delta_F)\left(1 - \frac{\lambda_a^2 \Delta_q(\sin^4\theta + \cos^4\theta)}{4\tilde{\Delta}_q}\right), \quad
\Lambda_2 = (\Delta - \Delta_F)\left(1 - \frac{\lambda_b^2 \Delta_q(\sin^4\theta + \cos^4\theta)}{4\tilde{\Delta}_q}\right), \\
\Lambda_3 &= J - \frac{\sqrt{(\Delta + \Delta_F)(\Delta - \Delta_F)}\lambda_a\lambda_b\Delta_q(\sin^4\theta + \cos^4\theta)}{4\tilde{\Delta}_q}, \quad
\Lambda_4 = -\frac{(\Delta + \Delta_F)\lambda_a^2\Delta_q\sin^2\theta\cos^2\theta}{4\tilde{\Delta}_q}, \\
\Lambda_5 &= -\frac{(\Delta - \Delta_F)\lambda_b^2\Delta_q\sin^2\theta\cos^2\theta}{4\tilde{\Delta}_q}, \quad
\Lambda_6 = -\frac{\sqrt{(\Delta + \Delta_F)(\Delta - \Delta_F)}\lambda_a\lambda_b\Delta_q\sin^2\theta\cos^2\theta}{2\tilde{\Delta}_q}.
\end{aligned}
\tag{S32}
$$

S3. PHASE TRANSITION BOUNDARIES

A. First-order phase transition boundary

In this section, we derive the first-order phase transition boundary for the superradiant phase transition. Starting from Eq. (S11), we impose a constraint that the square root term must be greater than or equal to zero, resulting in the condition:

$$
h_1^2(4G^2 - \kappa^2) - h_2^2\kappa^2 \geq 2h_1 h_2,
\tag{S33}
$$

where $h_1 = \Delta_+(\Delta_-^2 + \kappa^2)\lambda_a^2$ and $h_2 = \Delta_-(\Delta_+^2 - 4G^2 + \kappa^2)\lambda_b^2$. We can set this condition with an equal sign to obtain the critical ratio between the atom-field couplings λ_{ac} and λ_{bc} as follows:

$$
\chi_c = \frac{\lambda_{bc}}{\lambda_{ac}} = \frac{\sqrt{2G - \kappa}\sqrt{(\Delta + \Delta_F)((\Delta - \Delta_F)^2 + \kappa^2)}}{\sqrt{(\Delta - \Delta_F)\kappa((\Delta + \Delta_F)^2 - 4G^2 + \kappa^2)}}.
\tag{S34}
$$

This ratio χ_c defines the first-order superradiant phase transition boundary in the λ_a–λ_b phase space. To ensure that χ_c is a real number, the pump strength G must satisfy the condition:

$$
\frac{\kappa}{2} < G < \frac{\sqrt{(\Delta + \Delta_F)^2 + \kappa^2}}{2}.
\tag{S35}
$$

From the condition in Eq. (S33), we can derive the critical pump strength for the first-order phase transition, denoted as $G_{\rm c}^{\rm 1st}$,

$$G_{\rm c}^{\rm 1st} = \frac{1}{4\Delta_-\kappa\lambda_b^2} \left\{ -\Delta_+(\Delta_-^2 + \kappa^2)\lambda_a^2 + \sqrt{\left[\Delta_+(\Delta_-^2 + \kappa^2)\lambda_a^2 + 2\Delta_-\kappa^2\lambda_b^2\right]^2 + 4\Delta_+^2\Delta_-^2\kappa^2\lambda_b^4} \right\}. \tag{S36}$$

In the special case where $\lambda_a = \lambda_b = \lambda$, the above equation simplifies to

$$G_{\rm c}^{\rm 1st} = \frac{1}{4\Delta_-\kappa} \left\{ -\Delta_+(\Delta_-^2 + \kappa^2) + \sqrt{\left[\Delta_+(\Delta_-^2 + \kappa^2) + 2\Delta_-\kappa^2\right]^2 + 4\Delta_+^2\Delta_-^2\kappa^2} \right\}, \tag{S37}$$

which is Eq. (3) in the main text.

B. Second-order phase transition boundary

In order to explore the second-order phase transition boundary of the system, we start with Eq. (S17) and derive the dynamic equation for the first-order bosonic moments

$$\dot{\mathbf{L}}_{\rm np} = \Sigma_{\rm np}\mathbf{L}_{\rm np}, \tag{S38}$$

where $\mathbf{L}_{\rm np} = [\langle a\rangle, \langle a^\dagger\rangle, \langle b\rangle, \langle b^\dagger\rangle]^{\rm T}$ and

$$\Sigma_{\rm np} = \begin{pmatrix} -i\Delta_a - \kappa & -2iG & -iJ_s & 0 \\ 2iG & i\Delta_a - \kappa & 0 & iJ_s \\ -iJ_s & 0 & -i\Delta_b - \kappa & 0 \\ 0 & iJ_s & 0 & i\Delta_b - \kappa \end{pmatrix}, \tag{S39}$$

where Δ_a, Δ_b and J_s have been defined in Eq. (S18). Diagonalizing the matrix $\Sigma_{\rm np}$ and setting the real part of the eigenvalues to zero, we obtain that for a certain G, the two critical atom-field couplings λ_{ac} and λ_{bc} satisfy:

$$\lambda_{bc} = \frac{\left\{4q_1\Delta_- - \Delta_+(\Delta_+\Delta_- + \kappa^2)\lambda_{ac}^2 - 2\left[4\kappa^2 q_1(\Delta_F\Delta_+\lambda_{ac}^2 - q_1) + \Delta_+^2\left(\Delta_-^2 G^2 + (G^2 - \Delta_F^2)\kappa^2\right)\lambda_{ac}^4\right]^{1/2}\right\}^{1/2}}{q_1\Delta_-}, \tag{S40}$$

where $q_1 = \Delta_+^2 - 4G^2 + \kappa^2$. Equation (S40) gives the second-order phase transition boundary in the λ_a–λ_b phase space.

In Fig. S1 we plot the order parameters $\alpha_{\rm re}, \alpha_{\rm im}, \beta_{\rm re}, \beta_{\rm im}$ for the forward [panels (a)-(d)] and backward [panels (e)-(h)] pump cases. For each fixed pump direction, the order parameters exhibit similar features and share the same boundary. The system undergoes phase transitions from the normal phase (NP) to the superradiant phase (SP) through two distinct paths: one is through the first-order phase transition boundary (indicated by the gray dashed line) where the order parameters undergo an abrupt and discontinuous change from zero to a finite value (as given by Eq. (S34)); the other path is through the second-order phase transition boundary (magenta dash-dotted curve), where the order parameters vary continuously from zero to a finite value as λ_a or λ_b increases [as given by Eq. (S40)]. The first- and second-order phase transition boundaries meet at the tricritical point (see below). It is worth noting that the phase diagram of the order parameters exhibits *different* boundaries for *different* pump directions at a fixed pump strength. This *nonreciprocal* nature of the phase transition highlights the dependence of the system's behavior on the pump direction.

In the case of tuned atom-field couplings where $\lambda_a = \lambda_b = \lambda$, the eigenvalues of $\Sigma_{\rm np}$ are given by

$$E_{\rm np,\pm}^{(1)} = -\kappa \pm \frac{\left\{16G^2 + 4\Delta_F^2 p - \Delta^2(p^2 + 4) - \left[(\Delta^4\lambda^4 - 32\Delta\Delta_F G^2 - 8\Delta^2\Delta_F^2 p)(p-2)^2 - 16G^2\lambda^4\Delta_+\Delta_- + 256G^4\right]^{1/2}\right\}^{1/2}}{2\sqrt{2}}, \tag{S41}$$

$$E_{\rm np,\pm}^{(2)} = -\kappa \pm \frac{\left\{16G^2 + 4\Delta_F^2 p - \Delta^2(p^2 + 4) + \left[(\Delta^4\lambda^4 - 32\Delta\Delta_F G^2 - 8\Delta^2\Delta_F^2 p)(p-2)^2 - 16G^2\lambda^4\Delta_+\Delta_- + 256G^4\right]^{1/2}\right\}^{1/2}}{2\sqrt{2}}, \tag{S42}$$

with $p = \lambda^2 - 2$. Setting the real part of the eigenvalues equal to zero, i.e., $\mathrm{Re}[E_{\rm np}] = 0$, we obtain the critical pump
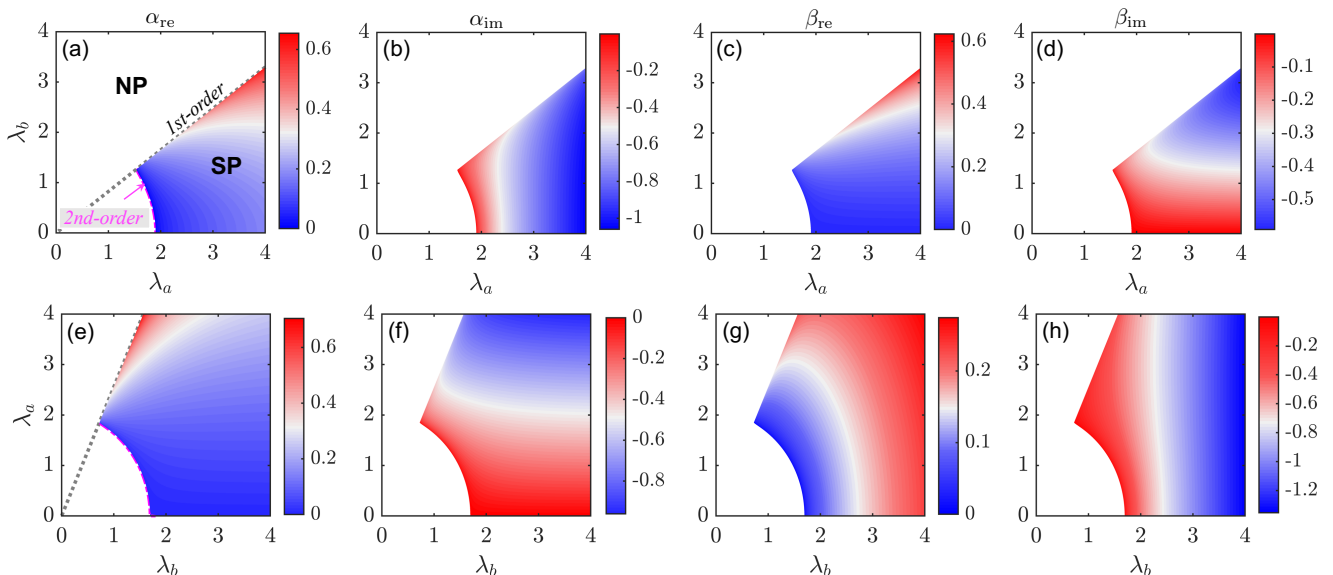
FIG. S1: Order parameters $\alpha_{\rm re}, \alpha_{\rm im}, \beta_{\rm re}, \beta_{\rm im}$ as functions of the atom-field couplings λ_a and λ_b for the forward (a-d) and backward (e-h) pumps. The gray dotted line and magenta dash-dotted curves denote the first-order [see Eq. (S34)] and second-order [see Eq. (S40)] phase transition boundaries, respectively. We consider $G/\kappa = 1.5$ for both cases, and $\Delta_F/\Delta = 0.5$ for the forward pump, and $\Delta_F/\Delta = -0.5$ for the backward pump, respectively. All other parameters are the same as in Fig. 1 of the main text.

strength for the second-order phase transition

$$G_c^{\rm 2nd} = \frac{\left\{\Delta^4(\lambda^2-2)^2 + \left(2\kappa^2 - \Delta_F^2(\lambda^2-2)\right)^2 + \Delta^2\left[\kappa^2((\lambda^2-2)^2+4) - 2\Delta_F^2(\lambda^2-2)^2\right]\right\}^{1/2}}{\left[16\kappa^2 + (\Delta-\Delta_F)^2(\lambda^2-4)^2\right]^{1/2}}, \tag{S43}$$

which is Eq. (4) of the main text. In Fig. S2(a), we illustrate $G_c^{\rm 1st}$ and $G_c^{\rm 2nd}$ as a function of the Sagnac shift Δ_F. The interplay of cavity rotation and directional pumping induces opposite Sagnac shifts, consequently causing the critical points moving towards larger (or smaller) values for the forward (or backward) pump.

The tricritical point is the intersection point where the first- and second-order boundaries meet. By setting $G_c^{\rm 1st} = G_c^{\rm 2nd}$, we can determine the atom-field coupling of the tricritical point,

$$\lambda_{\rm tric} = \left(\frac{\Delta_-^2 + \kappa^2}{\Delta_-^3(\Delta_+\Delta_- + \kappa^2)}\right)^{1/2}\left[3\Delta_-^2\Delta_+ - (\Delta_F-3\Delta)\kappa^2 - \left(\Delta_-^4\Delta_+^2 + 2\Delta_-^2\Delta_+(5\Delta+\Delta_F)\kappa^2 + (\Delta_F-3\Delta)^2\kappa^4\right)^{1/2}\right]^{1/2}. \tag{S44}$$

If the fixed coupling $\lambda > \lambda_{\rm tric}$ (or $\lambda < \lambda_{\rm tric}$), surpassing the critical pump $G_c^{\rm 1st}$ (or $G_c^{\rm 2nd}$) can trigger a first- (or second-) order phase transition. In our considered parameter regime, where $\kappa/\Delta \sim 0.01$ and $-\Delta < \Delta_F < \Delta$, the equation for the atom-field coupling at the tricritical point can be simplified as:

$$\lambda_{\rm tric} \approx \sqrt{\frac{2(\Delta+\Delta_F)[(\Delta-\Delta_F)^2+\kappa^2]}{(\Delta-\Delta_F)[(\Delta+\Delta_F)(\Delta-\Delta_F)+\kappa^2]}} \approx \sqrt{2}. \tag{S45}$$

In Fig. S2, we plot the difference between $\lambda_{\rm tric}$ and $\sqrt{2}$. It can be seen that this difference is on the order of 10^{-3} in our considered parameter regime, which is consistent with the analytical result given in Eq. (S45). In other words, in our model, the atom-field coupling at the tricritical point is insensitive to the Sagnac shift.
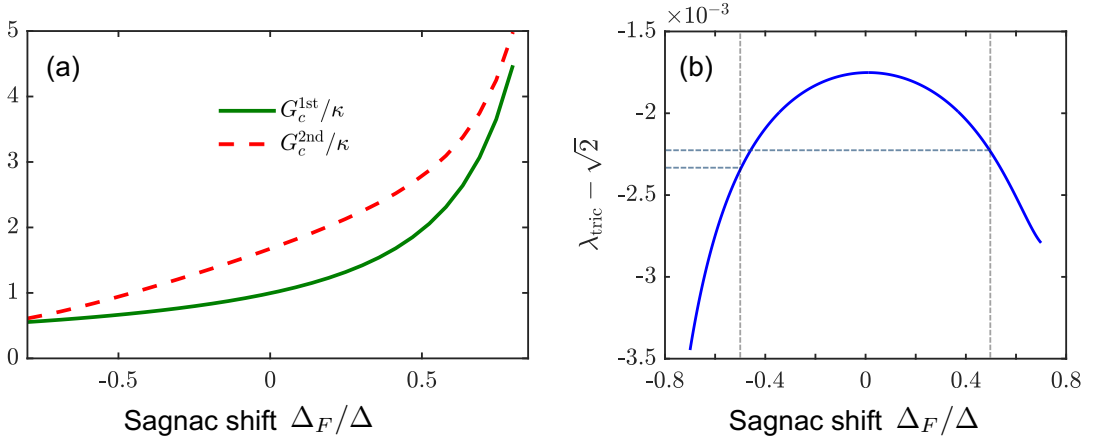
FIG. S2: (a) The first-order and second-order critical pumps G_c^{1st} and G_c^{2nd} versus the Sagnac shift Δ_F. (b) The atom-field coupling strength λ_{tric} of the tricritical point minus $\sqrt{2}$ as a function of the Sagnac shift Δ_F. The parameters used $\Delta_F/\Delta = \pm 0.5$ are labeled with the dotted curves.

S4.   DYNAMIC EVOLUTION OF TWO-OPERATOR CORRELATORS

A.   Equations of motion in the normal phase

To be consistent with the operator representation used in the main text, we perform a displacement on the cavity fields, i.e., $a \to c + \alpha\sqrt{\eta_+}$, $b \to d + \beta\sqrt{\eta_-}$, where c and d are cavity fluctuation operators. In the normal phase, $\alpha = \beta = 0$. Using the equation $\partial\langle o\rangle/\partial t = \text{tr}\{o\partial\rho/\partial t\}$ for the expectation value $\langle o\rangle = \text{tr}\{o\rho\}$ of any observable o of interest, and utilizing Eq. (S17), we can obtain a set of closed equations of the motion for the two-operator fluctuation correlators. These equations take the following form:

$$\frac{d\mathbf{v}_{np}}{dt} = W_{np}\mathbf{v}_{np} + R_{np}, \tag{S46}$$

where $\mathbf{v}_{np} = [\langle c^\dagger c\rangle, \langle c^{\dagger 2}\rangle, \langle c^2\rangle, \langle cd\rangle, \langle c^\dagger d^\dagger\rangle, \langle cd^\dagger\rangle, \langle c^\dagger d\rangle, \langle d^\dagger d\rangle, \langle d^2\rangle, \langle d^{\dagger 2}\rangle]^T$, $R_{np} = [0, 2iG, -2iG, 0, 0, 0, 0, 0, 0, 0]^T$, and

$$W_{np} = \begin{pmatrix} W_{np}^{(1,1)} & W_{np}^{(1,2)} \\ W_{np}^{(2,1)} & W_{np}^{(2,2)} \end{pmatrix} \tag{S47}$$

with

$$W_{np}^{(1,1)} = \begin{pmatrix} -2\kappa & -2iG & 2iG & 0 & 0 \\ 4iG & 2i\Delta_a-2\kappa & 0 & 0 & 2iJ_s \\ -4iG & 0 & -2i\Delta_a-2\kappa & -2iJ_s & 0 \\ 0 & 0 & -iJ_s & -i(\Delta_a+\Delta_b)-2\kappa & 0 \\ 0 & iJ_s & 0 & 0 & i(\Delta_a+\Delta_b)-2\kappa \end{pmatrix},$$

$$W_{np}^{(1,2)} = \begin{pmatrix} iJ_s & -iJ_s & 0 & 0 & 0 \\ 0 & 0 & 0 & 0 & 0 \\ 0 & 0 & 0 & 0 & 0 \\ 0 & -2iG & 0 & -iJ_s & 0 \\ 2iG & 0 & 0 & 0 & iJ_s \end{pmatrix}, W_{np}^{(2,1)} = \begin{pmatrix} iJ_s & 0 & 0 & 0 & -2iG \\ -iJ_s & 0 & 0 & 2iG & 0 \\ 0 & 0 & 0 & 0 & 0 \\ 0 & 0 & 0 & -2iJ_s & 0 \\ 0 & 0 & 0 & 0 & 2iJ_s \end{pmatrix},$$

$$W_{\mathrm{np}}^{(2,2)} = \begin{pmatrix} -i(\Delta_a - \Delta_b) - 2\kappa & 0 & -iJ_s & 0 & 0 \\ 0 & i(\Delta_a - \Delta_b) - 2\kappa & iJ_s & 0 & 0 \\ -iJ_s & iJ_s & -2\kappa & 0 & 0 \\ 0 & 0 & 0 & -2i\Delta_b - 2\kappa & 0 \\ 0 & 0 & 0 & 0 & 2i\Delta_b - 2\kappa \end{pmatrix},$$

In the steady state, we can solve Equation (S46) by setting the left-hand side to zero, yielding the following expression for the ten two-operator correlators in the steady state:

$$\mathbf{v}_{\mathrm{np}} = -W_{\mathrm{np}}^{-1} R_{\mathrm{np}}.$$

The analytical expressions of these correlators are complex and not presented here, but their numerical results are shown in Figs. 3(a)-3(c) in the main text.

B. Equations of motion in the superradiant phase

To derive the dynamic equation for the two-operator fluctuation correlators in the superradiant phase, we start with the equation of motion for the reduced density matrix in the superradiant phase, given by

$$\dot{\rho}_{\mathrm{sp}} = -i[H_{\mathrm{sp}}, \rho_{\mathrm{sp}}] + \kappa(2c\rho_{\mathrm{sp}}c^\dagger - c^\dagger c\rho_{\mathrm{sp}} - \rho_{\mathrm{sp}}c^\dagger c) + \kappa(2d\rho_{\mathrm{sp}}d^\dagger - d^\dagger d\rho_{\mathrm{sp}} - \rho_{\mathrm{sp}}d^\dagger d). \tag{S48}$$

Here, $\rho_{\mathrm{sp}} = \langle \tilde{\downarrow} | \tilde{\rho} | \tilde{\downarrow} \rangle$ represents the reduced density matrix in the superradiant phase. Using the equation $\partial \langle o \rangle / \partial t = \mathrm{tr}\{o \partial \rho / \partial t\}$ for the expectation value $\langle o \rangle = \mathrm{tr}\{o\rho\}$, we can express the time derivative of the two-operator fluctuation correlators as follows:

$$\frac{d\langle c^\dagger c \rangle}{dt} = 2i(G + \Lambda_4 e^{2i\phi})\langle c^2 \rangle - 2i(G + \Lambda_4 e^{-2i\phi})\langle c^{\dagger 2} \rangle + i\Lambda_3(\langle cd^\dagger \rangle - \langle c^\dagger d \rangle) + i\Lambda_6(e^{2i\phi}\langle cb \rangle - e^{-2i\phi}\langle c^\dagger d^\dagger \rangle) - 2\kappa\langle c^\dagger c \rangle, \tag{S49}$$

$$\frac{d\langle c^{\dagger 2} \rangle}{dt} = 2i(\Lambda_1 + i\kappa)\langle c^{\dagger 2} \rangle + 2i(G + \Lambda_4 e^{2i\phi})(2\langle c^\dagger c \rangle + 1) + 2i\Lambda_3\langle c^\dagger d^\dagger \rangle + 2i\Lambda_6 e^{2i\phi}\langle c^\dagger d \rangle, \tag{S50}$$

$$\frac{d\langle c^2 \rangle}{dt} = -2i(\Lambda_1 - i\kappa)\langle c^2 \rangle - 2i(G + \Lambda_4 e^{-2i\phi})(2\langle c^\dagger c \rangle + 1) - 2i\Lambda_3\langle cd \rangle - 2i\Lambda_6 e^{-2i\phi}\langle cd^\dagger \rangle, \tag{S51}$$

$$\frac{d\langle cd \rangle}{dt} = -i(\Lambda_1 + \Lambda_2 - 2i\kappa)\langle cd \rangle - 2i(G + \Lambda_4 e^{-2i\phi})\langle c^\dagger d \rangle - i\Lambda_3(\langle c^2 \rangle + \langle d^2 \rangle)) - 2i\Lambda_5 e^{-2i\phi}\langle cd^\dagger - i\Lambda_6 e^{-2i\phi}\langle d^\dagger d \rangle - i\Lambda_6 e^{-2i\phi}(\langle c^\dagger c \rangle + 1), \tag{S52}$$

$$\frac{d\langle c^\dagger d^\dagger \rangle}{dt} = i(\Lambda_1 + \Lambda_2 + 2i\kappa)\langle c^\dagger d^\dagger \rangle + 2i(G + \Lambda_4 e^{2i\phi})\langle cd^\dagger \rangle + i\Lambda_3(\langle c^{\dagger 2} \rangle + \langle d^{\dagger 2} \rangle)) + 2i\Lambda_5 e^{2i\phi}\langle c^\dagger d + i\Lambda_6 e^{2i\phi}(\langle d^\dagger d \rangle + 1) + i\Lambda_6 e^{2i\phi}\langle c^\dagger c \rangle, \tag{S53}$$

$$\frac{d\langle cd^\dagger \rangle}{dt} = -i(\Lambda_1 - \Lambda_2 - 2i\kappa)\langle cd^\dagger \rangle - 2i(G + \Lambda_4 e^{-2i\phi})\langle c^\dagger d^\dagger \rangle + i\Lambda_3(\langle c^\dagger c \rangle - \langle d^\dagger d \rangle) + 2i\Lambda_5 e^{2i\phi}\langle cd \rangle - i\Lambda_6(e^{-2i\phi}\langle d^{\dagger 2} \rangle - e^{2i\phi}\langle c^2 \rangle), \tag{S54}$$

$$\frac{d\langle c^\dagger d \rangle}{dt} = i(\Lambda_1 - \Lambda_2 + 2i\kappa)\langle c^\dagger d \rangle + 2i(G + \Lambda_4 e^{2i\phi})\langle cd \rangle - i\Lambda_3(\langle c^\dagger c \rangle - \langle d^\dagger d \rangle) - 2i\Lambda_5 e^{-2i\phi}\langle c^\dagger d^\dagger \rangle + i\Lambda_6(e^{2i\phi}\langle d^2 \rangle - e^{-2i\phi}\langle c^{\dagger 2} \rangle), \tag{S55}$$

$$\frac{d\langle d^\dagger d \rangle}{dt} = -i\Lambda_3(\langle cd^\dagger \rangle - \langle c^\dagger d \rangle) + i\Lambda_6(e^{2i\phi}\langle cd \rangle - e^{-2i\phi}\langle c^\dagger d^\dagger \rangle) + 2i\Lambda_5(e^{2i\phi}\langle d^2 \rangle - e^{-2i\phi}\langle d^{\dagger 2} \rangle) - 2\kappa\langle d^\dagger d \rangle, \tag{S56}$$

$$\frac{d\langle d^2 \rangle}{dt} = -2i(\Lambda_2 + i\kappa)\langle d^2 \rangle - 2i\Lambda_3\langle cd \rangle - 2i\Lambda_6 e^{-2i\phi}\langle c^\dagger d \rangle - 2i\Lambda_5 e^{-2i\phi}(2\langle d^\dagger d + 1), \tag{S57}$$

$$\frac{d\langle d^{\dagger 2} \rangle}{dt} = 2i(\Lambda_2 + i\kappa)\langle d^{\dagger 2} \rangle + 2i\Lambda_3\langle c^\dagger d^\dagger \rangle + 2i\Lambda_6 e^{2i\phi}\langle cd^\dagger \rangle + 2i\Lambda_5 e^{2i\phi}(2\langle d^\dagger d \rangle + 1). \tag{S58}$$

We solve these ten coupled equations to obtain the cavity fluctuation $\langle c^\dagger c \rangle$ or $\langle d^\dagger d \rangle$ in the steady state, as shown in Figs. 3(a)-3(c) in the main text.

S5. STABILITY ANALYSIS

In this section, we discuss the stability of the system. Starting with the Heisenberg equations (S2-S6), we perform a semiclassical analysis. Specifically, we set $\langle \sigma_x \rangle = X$, $\langle \sigma_y \rangle = Y$, $\langle \sigma_z \rangle = Z$, $\langle a \rangle = \alpha\sqrt{\eta_+}$, $\langle b \rangle = \beta\sqrt{\eta_-}$. Furthermore, we expand the order parameters as $\alpha \to \alpha + \delta\alpha, \beta \to \beta + \delta\beta$ and $X \to X + \delta X, Y \to Y + \delta Y, Z \to Z + \delta Z$, where α, β, X, Y, Z are the mean-field steady-state solutions shown in Sec. S1, and $\delta\alpha, \delta\beta, \delta X, \delta Y, \delta Z$ are quantum fluctuations. These expansions are valid in the limits of $\Delta_q/(\Delta \pm \Delta_F)$ and $\Delta_q/G \to \infty$. The equations of motion for

the quantum fluctuations satisfy

$$\dot{\mathbf{u}} = M\mathbf{u},$$

with $\mathbf{u} = [\delta\alpha_{\mathrm{re}}, \delta\alpha_{\mathrm{im}}, \delta\beta_{\mathrm{re}}, \delta\beta_{\mathrm{im}}, \delta X, \delta Y]^{\mathrm{T}}$ and the stability matrix M is given by
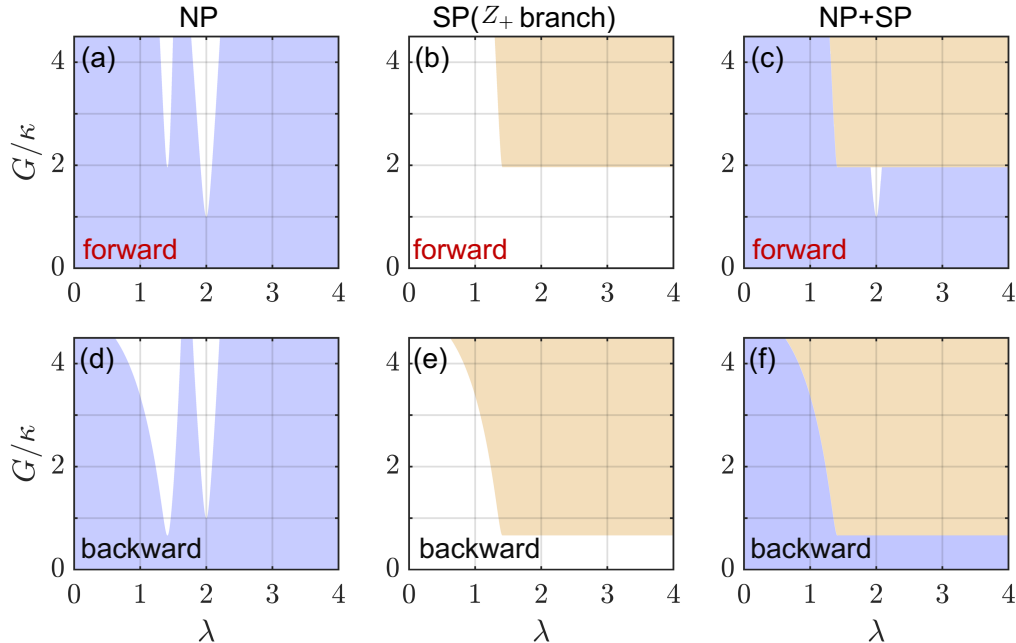

FIG. S3: Stability of the system for the forward and backward pumps in the normal phase (NP) and Z_+ branch of the superradiant phase (SP). The upper panels show the stability of the forward pump case, while the lower panels show the stability of the backward pump case. Panels (c,f) show the stability of the combination of the NP and SP. In the blank regions, the system is unstable. The parameter $\Delta_F/\Delta = 0.5$ for the forward pump and $\Delta_F/\Delta = -0.5$ for the backward pump. The values of Δ_q is 10^4, and the other parameters are the same as in Fig. 3 of the main text.

$$M = \begin{pmatrix} -\kappa & \Delta_+ - 2G & 0 & J\sqrt{\frac{\Delta_+}{\Delta_-}} & 0 & -\frac{1}{4}\lambda_a\Delta_+ \\ -(\Delta_+ + 2G) & -\kappa & -J\sqrt{\frac{\Delta_+}{\Delta_-}} & 0 & -\frac{1}{4}\lambda_a\Delta_+ & 0 \\ 0 & J\sqrt{\frac{\Delta_-}{\Delta_+}} & -\kappa & \Delta_- & 0 & -\frac{1}{4}\lambda_b\Delta_- \\ -J\sqrt{\frac{\Delta_-}{\Delta_+}} & 0 & -\Delta_- & -\kappa & -\frac{1}{4}\lambda_b\Delta_- & 0 \\ 0 & -\lambda_a\Delta_q Z & 0 & -\lambda_b\Delta_q Z & \frac{X}{Z}\Delta_q(\lambda_a\alpha_{\mathrm{im}} + \lambda_b\beta_{\mathrm{im}}) & \Delta_q[-1 + \frac{Y}{Z}(\lambda_a\alpha_{\mathrm{im}} + \lambda_b\beta_{\mathrm{im}})] \\ -\lambda_a\Delta_q Z & 0 & -\lambda_b\Delta_q Z & 0 & \Delta_q[1 + \frac{X}{Z}(\lambda_a\alpha_{\mathrm{re}} + \lambda_b\beta_{\mathrm{re}})] & \Delta_q\frac{Y}{Z}(\lambda_a\alpha_{\mathrm{re}} + \lambda_b\beta_{\mathrm{re}}) \end{pmatrix},$$

$$\text{(S59)}$$

where $\Delta_\pm = \Delta \pm \Delta_F$. During the stability analysis, we separated the mean-field solutions and quantum fluctuations into real and imaginary parts, namely, $\alpha = \alpha_{\mathrm{re}} + i\alpha_{\mathrm{im}}$, $\beta = \beta_{\mathrm{re}} + i\beta_{\mathrm{im}}$ and $\delta\alpha = \delta\alpha_{\mathrm{re}} + i\delta\alpha_{\mathrm{im}}$, $\delta\beta = \delta\beta_{\mathrm{re}} + i\delta\beta_{\mathrm{im}}$. The stability of the system is determined by the eigenvalues of the matrix M. If all eigenvalues have negative real parts, the system is stable and evolves into its steady state for $t \to \infty$.

Figure S3 shows the stable regions in the normal and superradiant phases for both forward and backward pump cases at $\Delta_q = 10^4$. We find that for the forward pump, there is an unstable region located in the vicinity of $\lambda = 2$ [see Fig. S3(c)]. However, for the backward pump case, this unstable region disappears, and both the normal and Z_+ branch of the superradiant phases are stable, as illustrated in Fig. S3(f). It is worth noting that the Z_- branch solution in the superradiant phase is unstable (not shown here).

S6. THE VALIDITY OF THE SEMICLASSICAL APPROACH

A. Overview

In Sec. S1, we derive the mean-field solutions of cavity occupations by applying a semiclassical approach. Here, we offer a comprehensive review of the semiclassical approach, focusing on scenarios where the field interacts with a *single* atom. The semiclassical approach has proven to be effective in investigating various phase-transition-like behaviors within the Rabi model. These include the ground-state quantum phase transition (QPT)[S1–S4], the excited-state QPT (ESQPT) indicated by the divergence of the semiclassical density of states[S5], dissipative QPT[S6], and the breakdown of the photon blockade[S7]. It is worth noting that, although the semiclassical approach may not precisely capture the diverging quantum fluctuation of the cavity field in the limit of infinite detuning ($\Omega/\omega_0 \to \infty$) in the Rabi model, it remains a reliable method for describing mean-field quantities such as the photon population and the atomic population of the ground state.

B. Analytical derivations

Here, we present an alternative yet intuitive derivation to illustrate that applying the semiclassical approximation solely to the cavity field leads to the semiclassical equations, aligning with the results presented in Sec. S1. We initiate the derivation with the master equation (2) in the main text and utilize the equation $\partial \langle O \rangle / \partial t = \text{Tr}\{O \partial \rho / \partial t\}$, where the expectation value is denoted as $\langle O \rangle = \text{Tr}\{O\rho\}$. Subsequently, we obtain the equations of motion as follows:

$$\dot{\langle a \rangle} = -i(\Delta + \Delta_F)\langle a \rangle - \kappa\langle a \rangle - 2iG\langle a^\dagger \rangle - iJ\langle b \rangle - \frac{i}{2}g_a\langle \sigma_x \rangle - \frac{1}{2}g_a\langle \sigma_y \rangle, \tag{S60}$$

$$\dot{\langle b \rangle} = -i(\Delta - \Delta_F)\langle b \rangle - \kappa\langle b \rangle - iJ\langle a \rangle - \frac{i}{2}g_b\langle \sigma_x \rangle - \frac{1}{2}g_b\langle \sigma_y \rangle, \tag{S61}$$

$$\dot{\langle \sigma_x \rangle} = -\Delta_q\langle \sigma_y \rangle + ig_a(\langle a\sigma_z \rangle - \langle a^\dagger\sigma_z \rangle) + ig_b(\langle b\sigma_z \rangle - \langle b^\dagger\sigma_z \rangle), \tag{S62}$$

$$\dot{\langle \sigma_y \rangle} = \Delta_q\langle \sigma_x \rangle - g_a(\langle a\sigma_z \rangle + \langle a^\dagger\sigma_z \rangle) - g_b(\langle b\sigma_z \rangle + \langle b^\dagger\sigma_z \rangle), \tag{S63}$$

$$\dot{\langle \sigma_z \rangle} = ig_a(\langle a^\dagger\sigma_x \rangle - \langle a\sigma_x \rangle) + ig_b(\langle b^\dagger\sigma_x \rangle - \langle b\sigma_x \rangle) + g_a(\langle a\sigma_y \rangle + \langle a^\dagger\sigma_y \rangle)$$
$$+ g_b(\langle b\sigma_y \rangle + \langle b^\dagger\sigma_y \rangle). \tag{S64}$$

The semiclassical (or mean-field) equations can be derived from the Eqs. (S60-S64) by assuming the vanishing of second cumulants. For instance, this assumption implies $\langle a\sigma_z \rangle = \langle a \rangle\langle \sigma_z \rangle$. Specifically, we express the cavity field operators as $a = \langle a \rangle + \delta a$ and $b = \langle b \rangle + \delta b$, where the fluctuation δa (or δb) is much smaller than the mean values $\langle a \rangle$ (or $\langle b \rangle$). When inserting the operator a into terms involving the second cumulants, for example, $\langle a\sigma_z \rangle = \langle (\langle a \rangle + \delta a)\sigma_z \rangle = \langle a \rangle\langle \sigma_z \rangle + \langle \delta a\sigma_z \rangle$, neglecting the quantum fluctuation $\langle \delta a\sigma_z \rangle$, then we obtain $\langle a\sigma_z \rangle = \langle a \rangle\langle \sigma_z \rangle$. That is, regarding the atomic part, we retain the terms $\langle \sigma_{x,y,z} \rangle$ because they are finite constants and follow the spin-conservation law $\langle \sigma_x \rangle^2 + \langle \sigma_y \rangle^2 + \langle \sigma_z \rangle^2 = 1$. This approach allows us to derive the same semiclassical equations as discussed in Sec. S1.

This approach can be validated through the low-energy Hamiltonian. As discussed in Sec. S2.B, in the large detuning limit where the atomic energy scale significantly exceeds the field part, we can decouple the atomic subspaces and concentrate on the lowest atomic subspace. Based on Eq. (S23), we can calculate the mean value of the operator σ_z in the lowest-energy state (or ground state) as follows:

$$\langle \tilde{\downarrow}|\sigma_z|\tilde{\downarrow} \rangle = -\frac{1}{\sqrt{1 + (\alpha_{\text{im}}^2 + \alpha_{\text{re}}^2)\lambda_a^2 + 2(\alpha_{\text{im}}\beta_{\text{im}} + \alpha_{\text{re}}\beta_{\text{re}})\lambda_a\lambda_b + (\beta_{\text{im}}^2 + \beta_{\text{re}}^2)\lambda_b^2}}, \tag{S65}$$

where α and β represent the mean-field solutions of the cavity occupations, and $\lambda_{a,b} = 2g_{a,b}/\sqrt{\Delta_q(\Delta \pm \Delta_F)}$ are dimensionless atom-field couplings of the Hamiltonian. When calculating $\langle \tilde{\downarrow}|\sigma_z|\tilde{\downarrow} \rangle$, the atomic part does not involve semiclassical approximation; only the cavity field is subjected to such an approximation.

In Fig. S4, we present the mean value of $\langle \sigma_z \rangle$ obtained from the mean-field approach (depicted by red circles) and $\langle \tilde{\downarrow}|\sigma_z|\tilde{\downarrow} \rangle$ derived from the full quantum description (illustrated by the black curve). Clearly, the mean values obtained from these two different methods are consistent, confirming the validity of applying semiclassical approximation solely to the cavity fields.

Based on the semiclassical equations (S60-S64), we can derive the steady-state mean amplitudes of the cavity fields $\langle a \rangle$, $\langle b \rangle$ and the atomic expectation values $\langle \sigma_x \rangle$, $\langle \sigma_y \rangle$ and $\langle \sigma_z \rangle$, see Sec. S1. Interestingly, we find that all of these steady-state quantities exhibit a bifurcation when the system parameter, specifically the pump strength (or
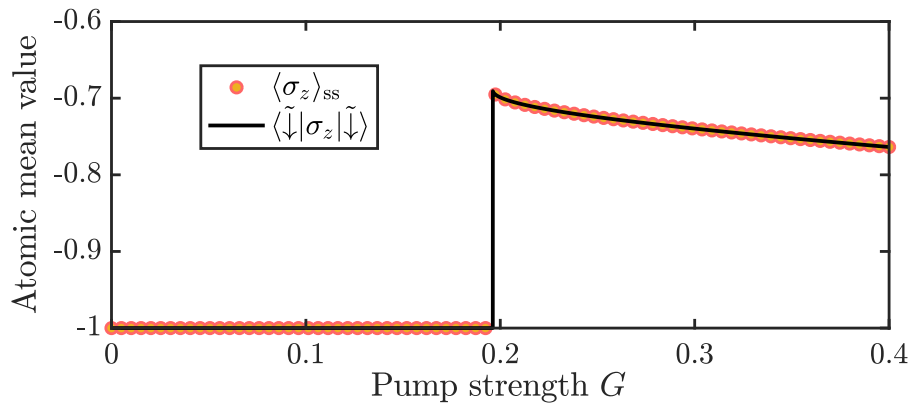
FIG. S4: The atomic expectation values as a function of the pump strength G. The red circles represent the atomic expectation value in the steady state $\langle \sigma_z \rangle$, and the black curve illustrates the atomic expectation value in the lowest-energy state $\langle \tilde{\downarrow} | \sigma_z | \tilde{\downarrow} \rangle$. The parameters considered here are $\Delta = 2, \Delta_F/\Delta = 0.5, \lambda_a = \lambda_b = 1.7, \kappa/\Delta = 0.05$.

atom-field coupling strength), is increased. We refer to the point where bifurcation occurs as the critical point for the second-order superradiant phase transition, denoted as $G_c^{2\text{nd}}$. It is worth noting that the critical point obtained through the semiclassical calculation aligns well with those derived from the full quantum description of the low-energy Hamiltonian in the infinite-detuning limit $\Delta_q/(\Delta \pm \Delta_F) \to \infty$, as discussed in Sections S2 and S3.B.
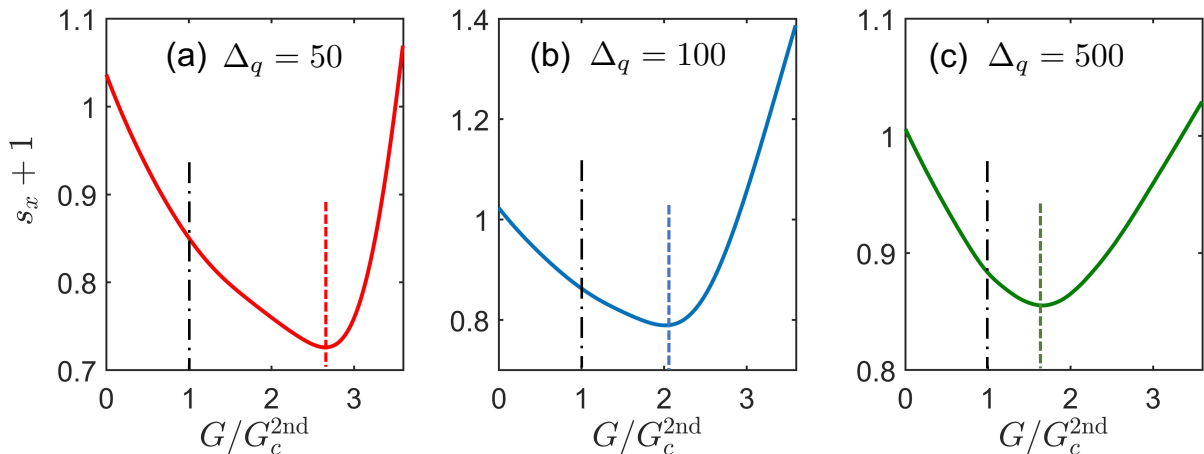

FIG. S5: Numerical calculation of the position-squeezing quantifier $s_x + 1$ as a function of $G/G_c^{2\text{nd}}$ for $\Delta_q = 50$ (a), 100 (b), 500 (c). Here, the analytical value of critical pump strength provided by the semiclassical approach, i.e., $G_c^{2\text{nd}}$, is denoted by the black dash–dotted line. Other parameters are same as Fig. 2(a,b) in the main text.

C. Squeezing parameter

To further illustrate the alignment of critical points obtained from the semiclassical approach and the full quantum approach, we begin with the master equation (2) in the main text and proceed to numerically calculate the position-squeezing parameter [S1, S2],

$$s_x = 2\langle (X - \langle X \rangle)^2 \rangle - 1,$$

where the quadrature variable is defined as $X = (a + a^\dagger)/\sqrt{2}$. In Figure S5, we plot the squeezing quantifier $s_x + 1$ as a function of the pump strength G (measured in comparison to the second-order critical pump strength $G_c^{2\text{nd}}$, which is the theoretical value obtained from the mean-field approach). As we increase the atomic detuning Δ_q (i.e., getting closer to the infinite detuning limit $\eta \to \infty$), the point where the squeezing quantifier reaches its minimum gradually

approaches the theoretical critical pump G_c^{2nd}. These numerical results indicate that by increasing the atomic detuning Δ_q, the critical pump converges towards the theoretical value provided by the mean-field approach [S1, S2].

S7. DISCUSSIONS ON THE DUAL-COUPLING JC MODEL

A. Comparison between the dual-coupling JC model and the Rabi model

Generally, the occurrence of the superradiant phase transition in the standard Rabi model, typically hinges on two critical conditions: (i) attaining an exceedingly large atomic frequency, such that $\omega_q/\omega \to \infty$, and (ii) achieving ultra-strong coupling between the atom and the field. Our model successfully overcomes the two critical challenging conditions present in the standard Rabi model. Specifically, for condition (i), in our model, the large atomic frequency was transformed into a large atomic detuning (i.e., $\Delta_q/\Delta \to \infty$, where $\Delta_q = \omega_q - \omega_p/2$ and $\Delta = \omega_0 - \omega_p/2$). By tuning the frequency of the pump field, one can readily achieve this large atomic detuning, which serves the same purpose as $\omega_q/\omega \to \infty$ in the standard Rabi model. Thus, condition (i) can be easily met in our model. Simultaneously, the critical atom-field coupling strength required for the onset of superradiant phase transitions is determined by the detunings Δ_q and Δ, rather than the atomic frequency ω_q and resonator frequency ω_0. Consequently, our proposed scheme can alleviate constraint (ii) from ultra-strong coupling to strong coupling.

B. Comparison between all-optical controls and its magnetic or electronic counterpart

In our model, the control over superradiant phase transitions and multicriticality is achieved through all-optical manipulation using external fields. This all-optical control presents several advantages in comparison to its magnetic and electronic counterparts. Firstly, in terms of integration, traditional methods for achieving optical nonreciprocity often rely on the magneto-optical Faraday effect [S8, S9]. These devices tend to be bulky and necessitate large magnetic fields, making them inconvenient for integration. Issues such as crosstalk induced by the magnetic field and lattice mismatches between magneto-optic materials and silicon further complicate integration [S10]. In contrast, our all-optical method for breaking system reciprocity demonstrates *high compatibility* and *ease of integration* into photonic systems. This characteristic not only enhances the potential for diverse applications in quantum communication but also provides essential building blocks for a quantum network [S11]. Secondly, all-optical systems are *more compact* than their magnetic and electronic counterparts. In our model, the microcavity is at the millimeter scale, and there have been reports of micrometer-scale optical cavities [S12]. This characteristic facilitates the development of on-chip nonreciprocal devices. Thirdly, all-optical system can be *easily reconfigured without need of the complex electronic components*. This characteristic makes opportunity to easily adjust the external pump strength for manipulating superradiant phase transitions and multicriticality. Fourthly, compared to the electronic counterparts, all-optical system, in general, can operate with *lower power consumption* [S13].

On the other hand, these advantages may stimulate further theoretical and experimental explorations, potentially advancing on-chip nonreciprocal device development. Our research reveals nonreciprocal superradiant phase transitions and a rich phase diagram featured by controllable multicritical points. These findings not only hold fundamental research significance but also provide quantum resources for quantum metrology [S14]. Therefore, our work may inspire the development of integrated high-precision quantum sensing. Moreover, extending our model to N- particle case may inspire many applications in optical field. Recently, steady-state superradiance has been demonstrated in a bad cavity regime, yielding lasing with a linewidth in the millihertz range [S15]. From this perspective, the combination of superradiance with our all-optical system may open up new avenues for designing on-chip unidirectional laser. Additionally, our system presents opportunities to explore and manipulate a broader range of physical phenomena, including superradiant cooling [S16] and atomic synchronization [S17]. This broadened scope enhances the versatility of our platform, offering unique opportunities for advancing our understanding and practical utilization of these intriguing phenomena.

S8. DISCUSSION ON THE ASSUMPTION OF SYSTEM PARAMETERS

A. The case of nonzero cavity hopping rate $J \neq 0$

In this section, we investigate how the cavity hopping rate J affects the superradiant transitions in the dual-coupling JC model. While the solutions for $J \neq 0$ have complicated mathematical expressions, we present here only
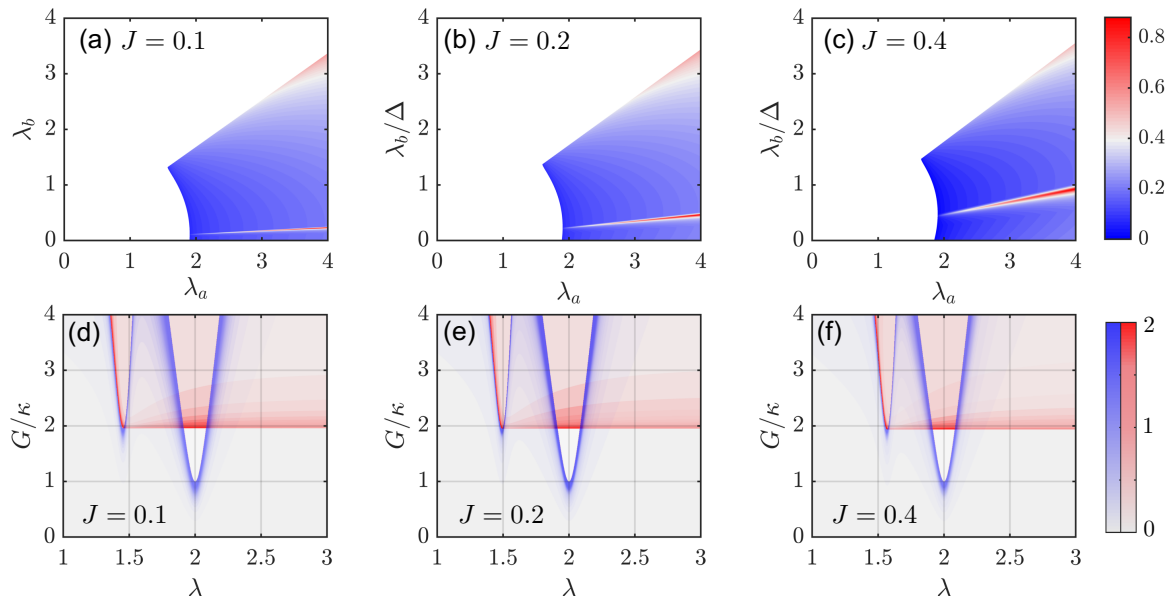
FIG. S6: (a-c) Phase diagram of the order parameter $\alpha_{\rm re}$ for different cavity hopping rate J. (d-e) Cavity fluctuation $\langle c^\dagger c \rangle$ as functions of λ and G. In all plots, we consider $\Delta_F/\Delta = 0.5$.

the numerical results. In Figs. S6(a)- S6(c) we plot the phase diagram of $\alpha_{\rm re}$ for different J. We observe that the non-zero value of J induces a continuous increase of $\alpha_{\rm re}$ in the bulk of the superradiant phase. Comparing with Fig. S1, we find that J causes only a small correction to the boundaries of the first- and second-order phase transitions. Moreover, from Figs. S6(d)- S6(f) we observe that the cone-shaped critical curve on the left shifts towards larger values of λ, which causes the critical point of the second-order transition to shift toward a larger pump strength G. Overall, we conclude that $J \neq 0$ does not alter the main physics discussed in our model.

B. Numerical simulations on steady-state mean photon number

In Fig. S7, we conducted numerical simulations to analyze the steady-state mean photon number $\langle a^\dagger a \rangle$ as a function of the pump strength G. These simulations are based on the full Hamiltonian (1) and the master equation (2), carried through the Qutip. The chosen system parameters for the simulations are as follows: cavity detuning $\Delta = 2$, cavity decay rate $\kappa/\Delta = 0.05$, atomic decay rate $\gamma = \kappa$, cavity hopping rate $J = \kappa$, and thermal photon number $\bar{n} = 7.4 \times 10^{-3}$. It is observed in Fig. S7 that for larger values of Δ_q, the growth in $\langle a^\dagger a \rangle$ occurs at a faster rate. As Δ_q/Δ increases, the tendency of $\langle a^\dagger a \rangle$ gradually approaches the case of infinite detuning limit, i.e., $\Delta_q/\Delta \to \infty$. In the infinite detuning limit, $\langle a^\dagger a \rangle$ diverges at the critical point. Note that due to the limited capabilities of computer, here, we have simulated only the case where Δ_q/Δ is maximally set to 50, with the cavity modes a and b truncated to 18. Even though, within reasonable experimental parameters, as we increase the atomic detuning value Δ_q/Δ, our numerical simulations, conducted without any assumptions and approximations, consistently converge towards the analytical results obtained for $\Delta_q/\Delta \to \infty$. This observation implies that our assumptions for the sake of analytical simplification are justified.

S9. POSSIBLE EXPERIMENTAL IMPLEMENTATIONS

To achieve nonreciprocal superradiant phase transitions and multicriticality, the possible experimental implementation relies on three techniques: first, reaching the strong-coupling regime in the interaction between the atom and cavity fields; second, unidirectionally squeezing one of the cavity modes; third, the capability to rotate the resonator. Recently, strong-coupling cavity QED has been realized using WGM microcavities, involving trapped atoms [S18–S24], quantum dots [S25–S28] and nitrogen-vacancy (NV) centers [S29, S30]. Combining these achievements with recent experiments on rotating resonator [S31] and optical squeezing [S32–S34], we discuss the feasibility of implementing our model with two potential setups: (i) cold cesium atoms falling onto the surface of a WGM microdisk cavity [S18–S21]
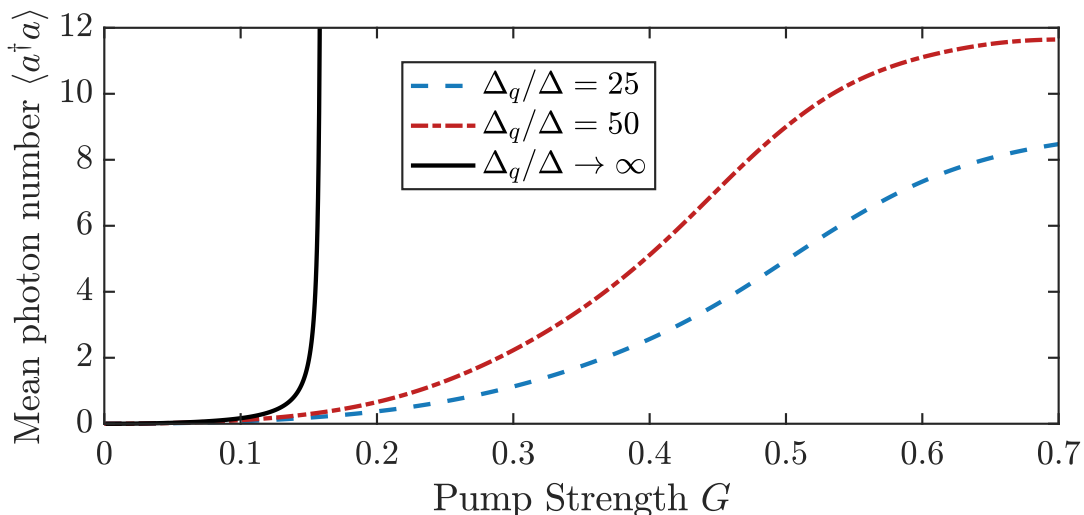
FIG. S7: Numerical simulation of the mean photon number $\langle a^\dagger a \rangle$ as a function of the pump strength G for finite detuning cases: $\Delta_q/\Delta = 25$ (depicted by the blue dotted curve) and $\Delta_q/\Delta = 50$ (illustrated by the red dash-dotted curve). The analytical result obtained for the infinite detuning case, $\Delta_q/\Delta \to \infty$, is shown by the black-solid curve. Here, we considered cavity decay $\kappa = 0.1$, atomic decay $\gamma = 0.1$, cavity hopping rate $J = 0.1$, and thermal photon number $\bar{n} = 7.4 \times 10^{-3}$. Due to computational limitations, simulations were conducted only for the case where Δ_q/Δ is maximally set to 50, with both cavity modes a and b truncated to 18. Additional parameters include $\Delta = 2$, $\Delta_F = 0$, $\lambda_a = \lambda_b = 1.4$.

and (ii) a single trapped ^{85}Rb atom interacting with a WGM microresonator [S22–S24]. Next, we provide detailed analysis of these experimental realization.

A. Strong coupling between an atom and microresonator

(i) cold cesium atoms falling onto the surface of a WGM microdisk

A possible experimental implementation platform could involve single cesium atoms radiatively coupled to a high-quality toroidal microresonator and in close proximity to the resonator's dielectric surface [S18–S21]. Specifically, a cloud of cold caesium atoms is located $\sim 800\,\mu$m above the surface of the resonator. Several caesium atoms are released from an optical dipole-force trap and fall within the evanescent field of cavity mode, establishing strong coupling to the resonator's field. Due to the aerodynamic process caused by the cavity rotation, the falling atom hovers a short distance above the rapidly rotating resonator instead of crashing into its surface [see Sec. S7. B]. This is distinct from the scenario involving a static resonator, as described by Refs. [S18, S21]. A real-time detection scheme, relying on strong radiative interactions between individual atoms and the evanescent cavity field, can be employed to select atomic trajectories passing within 300 nm from the resonator's surface. At this scale, the radiative atom-field interactions are characterized by strong coupling, evident in the observed vacuum-Rabi splitting. This experimental configuration can be theoretically modeled using the dual-coupling Jaynes-Cummings (JC) Hamiltonian, as demonstrated in Refs. [S18, S19, S21]. In these schemes, the average atom-photon coupling has been achieved at approximately 40 MHz, surpassing the dissipative rates of both the atom and the cavity, thereby reaching the strong-coupling regime.

(ii) a single trapped atom interacting with a WGM microresonator

Another possible experimental implementation platform could be trapping a single ^{85}Rb atom at a small distance from the surface of the WGM bottle microresonator [S22–S24]. The stable and controlled interaction between a single atom and the resonator in the strong-coupling regime (~ 10 MHz) is demonstrated in [S24]. Specifically, a single ^{85}Rb atom is trapped at a distance of about 200 nm from the resonator surface. This is achieved through a deep standing-wave optical dipole trap created by retroreflecting a focused trapping light field from the resonator surface. Additionally, a second, detuned compensation light field is employed to counteract the position-dependent detuning

of the atomic resonance from the resonator mode. Resonant detection light is sent through the coupling fiber to detect the presence of a single atom in the resonator mode in real-time, and the transmitted power is monitored using a single-photon counting module. The transmission signal is detected using a field-programmable gate array-based system. Upon detecting an atom, the detection light is switched off, and the dipole trap is switched on, with the overall delay between detection and trapping being approximately 250 ns. This duration is significantly shorter than the average transit time of an atom through the evanescent field of the resonator mode, enabling us to capture a detected atom if it is located inside the trapping volume.

B. Directionally squeezing of the cavity mode

With the advancement of nanofabrication techniques, a range of crystalline materials has been employed in the fabrication of WGM microresonators [S32–S38]. A notable advantage of crystalline cavities is their ability to support nonlinear optical processes, including optical parametric amplification (OPA). In a parametric amplifier, a pump beam interacting with a $\chi^{(2)}$ nonlinearity generates signal and idler beams. This OPA process is considered a crucial source of squeezed states of the radiative field.

Inspired by recent experiments, here we consider a crystalline WGM microresonator with high second-order nonlinearity. To ensure phase matching for parametric down-conversion along the entire circumference of the resonator, an uniaxial crystal with the optical axis along the symmetry axis of the cavity should be used. The microdisk can be fabricated from a 5% MgO-doped z-cut lithium niobate wafer, as demonstrated in Ref. [S32], or periodically poled lithium niobate, as demonstrated in Refs. [S33, S34]. The pump field interacts with the $\chi^{(2)}$ nonlinearity through a tapered fiber, generating a squeezed cavity mode. This is an optical parametric amplification process. The forward external light unidirectionally interacts with the clockwise $\chi^{(2)}$-nonlinearity, thereby directionally squeezing the clockwise cavity mode [S39]. In other words, the forward propagating mode through the waveguide selectively squeezes the copropagating mode in the resonator. Due to the rotation of the system, the light circulating in the resonator experiences a Sagnac-Fizeau shift, denoted by Δ_F.

C. Rotating resonator

The rotating scheme can be implemented by mounting the WGM resonator on a turbine, causing the resonator to rotate with a certain angular velocity. This setup has been demonstrated in a recent experiment by Maayani *et al.* [S31]. Positioning the rotating microresonator near a single-mode telecommunications fiber allows light to be evanescently coupled into or out of the resonator through the tapered region. It is worth noting that in this rotating scheme, the aerodynamic process plays a crucial role: a rapidly rotating resonator can drag air into the region between the taper and the microdisk, forming a boundary layer of air. Due to the air pressure on the surface of the taper facing the resonator, the taper hovers a short distance above the rapidly spinning resonator, avoiding direct contact or adherence to the resonator. This distinguishes it from the situation with a stationary resonator. If any disturbance causes the taper to ascend beyond its stable equilibrium height, it naturally returns to its original position, a phenomenon referred to as 'self-adjustment'.

D. Discussion on the effect of unexpected noises and perturbations

Based on the potential experimental implementations discussed above, we discuss how possible unexpected noises or perturbations might affect the performance of our system. The unexpected noises and perturbations may be attributed to the thermal noise of the cavity and the perturbations caused by the rotation scheme.

According to the experimentally feasible parameters, the cavity frequency is $\omega = 1.93 \times 10^{14}$ Hz. At room temperature $T = 300$ K, the thermal cavity number is $\bar{n} = 1/[\exp(\hbar\omega/k_B T) - 1] \approx 7.4 \times 10^{-3}$, which is significantly less than 1 and has been omitted in our analytical considerations. However, in plotting Fig. S7, we have considered non-zero thermal cavity number ($\bar{n} = 7.4 \times 10^{-3}$).

On the other hand, the rapidly rotating cavity drags a boundary layer of air around the resonator, which may induce the vibrations of the atom. This could alter the overlap between the atom and the mode volume of the resonator, modifying the atom-resonator coupling strength. However, as discussed in Sec. S9.A, the coupling strength between the WGM resonator and an atom in current experiments is sufficient to achieve nonreciprocal phase transitions in our model. Moreover, in our model, we achieve phase transitions by effectively enhancing the pump strength of the external field, and the Sagnac shift remains robust against modifications in coupling. Therefore, it is safe to say that this perturbation would not change the nonreciprocal behaviors of our model.

S10. EXTENDING THE MODEL TO THE CASE OF N PARTICLES ($N \gg 1$)

Our approach can be extended to scenarios involving an infinite number of atoms ($N \to \infty$), particularly within the context of the dual-coupling Tavis-Cummings (TC) model. Here, we give a brief discussion in this extension.

We consider N two-level atoms interacting with two counter-propagating modes of WGM resonator. The resonator is made of materials with second-order nonlinearity. A classical field with frequency ω_p input from the forward (or backward) can directionally generate squeezing cavity modes a (or b) through an optical parametric amplification process. The system Hamiltonian can be described by the dual-coupling TC model (in the forward pump):

$$H = \omega_0 a^\dagger a + \omega_0 b^\dagger b + \omega_q J_z + \frac{g_a}{\sqrt{N}}(aJ_+ + a^\dagger J_-) + \frac{g_b}{\sqrt{N}}(bJ_+ + b^\dagger J_-) + G(a^{\dagger 2}e^{-i\omega_p t} + a^2 e^{i\omega_p t}). \tag{S66}$$

Here $J_z = (1/2)\sum_{i=1}^{N} \sigma_z$ and $J_\pm = \sum_{i=1}^{N} \sigma_\pm$ represent collective angular-momentum operators. There are N atoms simultaneously coupled to cavity modes a and b with collective coupling strengths g_a and g_b, respectively. The cavity field is unidirectionally pumped by an external field with the pump strength of G. Additionally, we consider the microresonator rotates counterclockwise with an angular velocity Ω, causing the two cavity modes to experience Sagnac-Fizeau shifts with respect to their static resonance frequency ω_0, i.e., $\omega_0 \to \omega_0 \pm \Delta_F$. In the frame rotating at $\omega_p/2$, Hamiltonian (S66) is transformed into

$$H = (\Delta + \Delta_F)a^\dagger a + (\Delta - \Delta_F)b^\dagger b + \Delta_q J_z + \frac{g_a}{\sqrt{N}}(aJ_+ + a^\dagger J_-)$$
$$+ \frac{g_b}{\sqrt{N}}(bJ_+ + b^\dagger J_-) + G(a^{\dagger 2} + a^2), \tag{S67}$$

where the detunings are defined as $\Delta = \omega_0 - \omega_p/2$ and $\Delta_q = \omega_q - \omega_p/2$. The form of Hamiltonian (S67) closely resembles Hamiltonian (1) presented in the main text. Utilizing Hamiltonian (S67), we can derive mean field equations for $\langle a\rangle, \langle b\rangle, \langle J_{x,y,z}\rangle$ and subsequently calculate the critical points for both first-order and second-order superradiant phase transitions. This process aligns with the method employed in the manuscript.

The dual-coupling TC model maintains the advantages of the dual-coupling JC model. Firstly, from Hamiltonian (S67), we infer that the critical atom-field coupling strength necessary for the occurrence of superradiant phase transitions corresponds to the detunings Δ_q and Δ rather than the atomic frequency ω_q and resonator frequency ω_0. Thus, superradiant phase transitions in dual-coupling TC does not require ultra-strong atom-field coupling. Secondly, the dual-TC model, the condition of an extremely large detuning is transformed into the limit of an extremely large number of atoms, i.e., in the thermodynamic limit as $N \to \infty$. Thirdly, the control of superradiant phase transitions in the dual-TC model can also be achieved by adjusting the pump strength.

[S1] S. Ashhab and Franco Nori. Qubit-oscillator systems in the ultrastrong-coupling regime and their potential for preparing nonclassical states. *Phys. Rev. A*, 81:042311, Apr 2010.

[S2] S. Ashhab. Superradiance transition in a system with a single qubit and a single oscillator. *Phys. Rev. A*, 87:013826, Jan 2013.

[S3] Myung-Joong Hwang, Ricardo Puebla, and Martin B. Plenio. Quantum phase transition and universal dynamics in the Rabi model. *Phys. Rev. Lett.*, 115:180404, Oct 2015.

[S4] Maoxin Liu, Stefano Chesi, Zu-Jian Ying, Xiaosong Chen, Hong-Gang Luo, and Hai-Qing Lin. Universal scaling and critical exponents of the anisotropic quantum Rabi model. *Phys. Rev. Lett.*, 119:220601, Nov 2017.

[S5] Ricardo Puebla, Myung-Joong Hwang, and Martin B. Plenio. Excited-state quantum phase transition in the Rabi model. *Phys. Rev. A*, 94:023835, Aug 2016.

[S6] Myung-Joong Hwang, Peter Rabl, and Martin B. Plenio. Dissipative phase transition in the open quantum Rabi model. *Phys. Rev. A*, 97:013825, Jan 2018.

[S7] H. J. Carmichael. Breakdown of photon blockade: A dissipative quantum phase transition in zero dimensions. *Phys. Rev. X*, 5:031028, Sep 2015.

[S8] Zheng Wang, Yidong Chong, John D Joannopoulos, and Marin Soljačić. Observation of unidirectional backscattering-immune topological electromagnetic states. *Nature*, 461(7265):772–775, 2009.

[S9] Alexander B. Khanikaev, S. Hossein Mousavi, Gennady Shvets, and Yuri S. Kivshar. One-way extraordinary optical transmission and nonreciprocal spoof plasmons. *Phys. Rev. Lett.*, 105:126804, Sep 2010.

[S10] Daoxin Dai, Jared Bauters, and John E Bowers. Passive technologies for future large-scale photonic integrated circuits on silicon: polarization handling, light non-reciprocity and loss reduction. *Light: Science & Applications*, 1(3):e1–e1, 2012.

[S11] Gershon Kurizki, Patrice Bertet, Yuimaru Kubo, Klaus Mølmer, David Petrosyan, Peter Rabl, and Jörg Schmiedmayer. Quantum technologies with hybrid systems. *Proc. Natl. Acad. Sci. U. S. A.*, 112(13):3866–3873, 2015.

[S12] Jonathan Ward and Oliver Benson. WGM microresonators: sensing, lasing and fundamental optics with microspheres. *Laser & Photonics Reviews*, 5(4):553–570, 2011.

[S13] Masahiko Jinno and Takao Matsumoto. Ultrafast, low power, and highly stable all-optical switching in an all polarization maintaining fiber Sagnac interferometer. *IEEE Photonics Technol. Lett.*, 2:349–351, 1990.

[S14] Christoph Hotter, Helmut Ritsch, and Karol Gietka. Combining critical and quantum metrology. *Phys. Rev. Lett.*, 132:060801, Feb 2024.

[S15] Justin G Bohnet, Zilong Chen, Joshua M Weiner, Dominic Meiser, Murray J Holland, and James K Thompson. A steady-state superradiant laser with less than one intracavity photon. *Nature (London)*, 484(7392):78–81, 2012.

[S16] Minghui Xu, Simon B. Jäger, S. Schütz, J. Cooper, Giovanna Morigi, and M. J. Holland. Supercooling of atoms in an optical resonator. *Phys. Rev. Lett.*, 116:153002, Apr 2016.

[S17] Minghui Xu, D. A. Tieri, E. C. Fine, James K. Thompson, and M. J. Holland. Synchronization of two ensembles of atoms. *Phys. Rev. Lett.*, 113:154101, Oct 2014.

[S18] Takao Aoki, Barak Dayan, Elizabeth Wilcut, Warwick P Bowen, A Scott Parkins, TJ Kippenberg, KJ Vahala, and HJ Kimble. Observation of strong coupling between one atom and a monolithic microresonator. *Nature*, 443(7112):671–674, 2006.

[S19] Barak Dayan, AS Parkins, Takao Aoki, EP Ostby, KJ Vahala, and HJ Kimble. A photon turnstile dynamically regulated by one atom. *Science*, 319(5866):1062–1065, 2008.

[S20] Takao Aoki, A. S. Parkins, D. J. Alton, C. A. Regal, Barak Dayan, E. Ostby, K. J. Vahala, and H. J. Kimble. Efficient routing of single photons by one atom and a microtoroidal cavity. *Phys. Rev. Lett.*, 102:083601, Feb 2009.

[S21] D.J. Alton, N.P. Stern, Takao Aoki, Hansuek Lee, E. Ostby, K.J. Vahala, and H.J. Kimble. Strong interactions of single atoms and photons near a dielectric boundary. *Nat. Phys.*, 7(2):159–165, 2011.

[S22] Christian Junge, Danny O'Shea, Jürgen Volz, and Arno Rauschenbeutel. Strong coupling between single atoms and nontransversal photons. *Phys. Rev. Lett.*, 110:213604, May 2013.

[S23] Michael Scheucher, Adèle Hilico, Elisa Will, Jürgen Volz, and Arno Rauschenbeutel. Quantum optical circulator controlled by a single chirally coupled atom. *Science*, 354(6319):1577–1580, 2016.

[S24] Elisa Will, Luke Masters, Arno Rauschenbeutel, Michael Scheucher, and Jürgen Volz. Coupling a single trapped atom to a whispering-gallery-mode microresonator. *Phys. Rev. Lett.*, 126:233602, Jun 2021.

[S25] A Kiraz, P Michler, C Becher, B Gayral, A Imamoğlu, Lidong Zhang, E Hu, WV Schoenfeld, and PM Petroff. Cavity-quantum electrodynamics using a single InAs quantum dot in a microdisk structure. *Appl. Phys. Lett.*, 78(25):3932–3934, 2001.

[S26] E. Peter, P. Senellart, D. Martrou, A. Lemaître, J. Hours, J. M. Gérard, and J. Bloch. Exciton-photon strong-coupling regime for a single quantum dot embedded in a microcavity. *Phys. Rev. Lett.*, 95:067401, Aug 2005.

[S27] Kartik Srinivasan and Oskar Painter. Linear and nonlinear optical spectroscopy of a strongly coupled microdisk–quantum dot system. *Nature*, 450(7171):862–865, 2007.

[S28] Kartik Srinivasan and Oskar Painter. Mode coupling and cavity–quantum-dot interactions in a fiber-coupled microdisk cavity. *Phys. Rev. A*, 75:023814, Feb 2007.

[S29] Young-Shin Park, Andrew K Cook, and Hailin Wang. Cavity QED with diamond nanocrystals and silica microspheres. *Nano Lett.*, 6(9):2075–2079, 2006.

[S30] Russell J Barbour, Khodadad N Dinyari, and Hailin Wang. A composite microcavity of diamond nanopillar and deformed silica microsphere with enhanced evanescent decay length. *Optics Express*, 18(18):18968–18974, 2010.

[S31] Shai Maayani, Raphael Dahan, Yuri Kligerman, Eduard Moses, Absar U Hassan, Hui Jing, Franco Nori, Demetrios N Christodoulides, and Tal Carmon. Flying couplers above spinning resonators generate irreversible refraction. *Nature (London)*, 558(7711):569–572, 2018.

[S32] J. U. Fürst, D. V. Strekalov, D. Elser, A. Aiello, U. L. Andersen, Ch. Marquardt, and G. Leuchs. Quantum light from a whispering-gallery-mode disk resonator. *Phys. Rev. Lett.*, 106:113901, Mar 2011.

[S33] Juanjuan Lu, Joshua B Surya, Xianwen Liu, Alexander W Bruch, Zheng Gong, Yuntao Xu, and Hong X Tang. Periodically poled thin-film lithium niobate microring resonators with a second-harmonic generation efficiency of 250,000%/w. *Optica*, 6(12):1455–1460, 2019.

[S34] Juanjuan Lu, Ming Li, Chang-Ling Zou, Ayed Al Sayem, and Hong X Tang. Toward 1% single-photon anharmonicity with periodically poled lithium niobate microring resonators. *Optica*, 7(12):1654–1659, 2020.

[S35] Vladimir S. Ilchenko, Anatoliy A. Savchenkov, Andrey B. Matsko, and Lute Maleki. Nonlinear optics and crystalline whispering gallery mode cavities. *Phys. Rev. Lett.*, 92:043903, Jan 2004.

[S36] T. Beckmann, H. Linnenbank, H. Steigerwald, B. Sturman, D. Haertle, K. Buse, and I. Breunig. Highly tunable low-threshold optical parametric oscillation in radially poled whispering gallery resonators. *Phys. Rev. Lett.*, 106:143903, Apr 2011.

[S37] Michael Förtsch, Josef U Fürst, Christoffer Wittmann, Dmitry Strekalov, Andrea Aiello, Maria V Chekhova, Christine Silberhorn, Gerd Leuchs, and Christoph Marquardt. A versatile source of single photons for quantum information processing. *Nat. Commun.*, 4(1):1818, 2013.

[S38] Xiang Guo, Chang-Ling Zou, Hojoong Jung, and Hong X. Tang. On-chip strong coupling and efficient frequency conversion between telecom and visible optical modes. *Phys. Rev. Lett.*, 117:123902, Sep 2016.

[S39] Lei Tang, Jiangshan Tang, Mingyuan Chen, Franco Nori, Min Xiao, and Keyu Xia. Quantum squeezing induced optical nonreciprocity. *Phys. Rev. Lett.*, 128:083604, Feb 2022.